Multistatic Adaptive Microwave Imaging for Early Breast Cancer Detection

Yao Xie*, *Student Member, IEEE*, Bin Guo, *Student Member, IEEE*, Luzhou Xu, *Student Member, IEEE*, Jian Li, *Fellow, IEEE*, and Petre Stoica, *Fellow, IEEE*

***Abstract*—We propose a new multistatic adaptive microwave imaging (MAMI) method for early breast cancer detection. MAMI is a two-stage robust Capon beamforming (RCB) based image formation algorithm. MAMI exhibits higher resolution, lower sidelobes, and better noise and interference rejection capabilities than the existing approaches. The effectiveness of using MAMI for breast cancer detection is demonstrated via a simulated 3-D breast model and several numerical examples.**

***Index Terms*—Breast cancer detection, microwave imaging, multistatic, robust capon beamforming.**

I. INTRODUCTION

BREAST cancer persists to be the top threat to women's health. In the U.S. alone, in 2006 the number of new cases of breast cancer in women was estimated to be 212 920.[1] As explained in [1], early diagnosis is the key to beating the breast cancer. Hence detecting tumors at a nonpalpable early stage becomes the philosophy that drives the breast cancer screening technology. Although X-ray mammography remains the standard for tumor screening, its inherent limitations are also well recognized [2]. Among the emerging breast cancer imaging technologies, microwave imaging is one of the most promising and attractive methods. It is nonionizing, comfortable, sensitive to tumors, and specific to malignancies. The physical basis for microwave imaging lies in the significant contrast in the dielectric properties between the normal breast tissue and the malignant tissue at microwave frequencies [3]–[7].

During the past several decades, many modalities of microwave imaging have been considered [1], including passive, hybrid, and active approaches. The passive microwave imaging approaches mainly refer to the microwave radiometry [8], [9], which uses radiometers to measure temperature differences between the normal breast tissue and tumor due to their different metabolism rate. Hybrid methods use microwave to selectively heat tumors and ultrasound transducers to detect pressure waves generated by the expansion of the heated tissues [10]. The active methods include the tomography image reconstruction [11], [12] and the ultra-wideband (UWB) confocal microwave imaging (CMI) methods [13]. The tomography image reconstruction methods involve illuminating the breast with microwaves and then measuring transmitted or reflected microwave signals, to quantitative compute the spatial distributions of the dielectric constant and/or conductivity. UWB CMI is a more recent approach, where UWB microwave pulses are transmitted from antennas at different locations near the breast surface, the backscattered responses from the breast are recorded, and the backscattered energy distribution is calculated coherently. The advantages of UWB CMI include high-resolution resulting from the ultra-wide band signaling, as well as simple yet effective signal processing algorithms for image reconstruction.

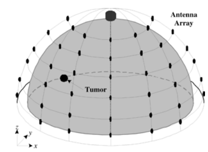

Fig. 1. Antenna array configuration.

Depending on how data is acquired, there are monostatic [13], bistatic [14], and multistatic [15], [16] CMI approaches. In the monostatic approach, the transmitter is also used as a receiver and is moved across the breast to form a synthetic aperture. For the bistatic approach, the transmitting and receiving antennas are different. In the multistatic approach, a real aperture array (see Fig. 1) is used for data collection. Each antenna in the array takes turns to transmit the probing pulse. For each transmitting antenna, all antennas in the array are used to receive the backscattered signals. The multistatic approach can give better imaging results than its monostatic or bistatic counterparts when the synthetic aperture formed by the latter two approaches is similar to the real aperture array used by the former. An intuitive explanation for this better performance is that the multistatic approach exploits multiple received signals that propagate via different routes, accruing more information about the tumor.

For monostatic and bistatic ultra-wideband CMI, the simple delay-and-sum (DAS) scheme [13], [15], the data-independent space-time beamforming (MIST) method [17], [18], and the data-adaptive robust Capon beamforming (RCB) method [14] as well as the amplitude and phase estimation (APES) algorithm [14] have been considered for image formation. The simulated breast models used to test these methods include

Manuscript received July 11, 2005; revised March 10, 2006. This work was supported in part by the National Science Foundation under Grant CCR-0104887 and in part by the Swedish Science Council (VR). *Asterisk indicates corresponding author.*

*Y. Xie is with the Department of Electrical and Computer Engineering, P. O. Box 116130, University of Florida, Gainesville, FL 32611 USA (e-mail: xieyao@dsp.ufl.edu).

B. Guo, L. Xu and J. Li are with the Department of Electrical and Computer Engineering, University of Florida, Gainesville, FL 32611 USA.

P. Stoica is with the Department of Information Technology, Systems and Control Division, Uppsala University, SE-75105 Uppsala, Sweden.

Color version of Figs. 2–8 are available online at http://ieeexplore.org

Digital Object Identifier 10.1109/TBME.2006.878058

[1]American Cancer Society. [Online]. Available: www.cancer.org.

a two-dimensional (2-D) model based on a breast magnetic resonance imaging scan, which was used with the monostatic DAS [13] and MIST [17], [18]; simple three-dimensional (3-D) cylindrical and planar models were used with the monostatic DAS [19], [20]; the more realistic 3-D hemispherical model was used with the monostatic DAS [21], [22] as well as RCB and APES [14]. For multistatic CMI, only DAS was considered so far for image formation using the simulated 2-D [15] and 3-D hemispherical breast models [22].

In this paper, we present a multistatic adaptive microwave imaging (MAMI) method for UWB CMI for early-stage breast cancer detection. MAMI employs the data adaptive RCB algorithm [23], [24] in two-stages. We use it with a realistic 3-D breast model to demonstrate its performance. The 3-D breast model is simulated using the finite-difference time-domain (FDTD) [25], [26] method. We show that MAMI has much better resolution and much better interference rejection capability than the existing methods.

The remainder of this paper is organized as follows. In Section II, we describe the pre-processing of the received signals, which precedes adaptive beamforming. Section III presents the MAMI algorithm for image formation. Numerical examples are presented in Section IV. Finally, Section V contains our conclusions.

II. Problem Formulation and Data Preprocessing

A. Problem Formulation

We consider a multistatic imaging system, where M antennas are arranged on a hemisphere relatively close to the breast skin, at known locations $\mathbf{r}_i = [x_i, y_i, z_i]^T$ $(i = 1, \ldots, M)$. Here, $(\cdot)^T$ denotes the transpose. The configuration of the array is shown in Fig. 1. The antennas are arranged on P layers with Q antennas per layer, where $M = PQ$. Each antenna takes turns to transmit an UWB probing pulse while all of the antennas record the backscattered signals. Let $E_{i,j}(t), i = 1, \ldots, M, j = 1, \ldots, M$, denote the backscattered signal generated by the probing pulse sent by the ith transmitting antenna and received by the jth receiving antenna. The 3×1 vectors $\mathbf{r}_{iT}$ and $\mathbf{r}_{jR}$ denote the locations of the ith transmitting and jth receiving antennas, respectively, and $\mathbf{r}_0$ denotes an imaging location.

Our goal herein is to form a 3-D image of the backscattered energy $p(\mathbf{r}_0)$ on a grid of points within the breast, with the goal of detecting the tumor. In our algorithm, the location $\mathbf{r}_0$ is varied to cover the entire grid points of the breast model. The backscattered energy is estimated from the complete received data $\{E_{i,j}(t)\}$ for each location $\mathbf{r}_0$ of interest.

B. Data Preprocessing

Before employing the MAMI for image formation, we preprocess the received signals to remove, as much as possible, backscattered signals (other than the tumor response), and to compensate for the propagation loss of the signal amplitude.

First, to remove the undesired content in the received signals, we use a removal method similar to that in [13]. Note that the received signals contain the tumor responses but also other backscattered signals, such as the incident pulse, reflections from the skin, fatty and glandular tissues and the chest wall, as well as parasitic signals due to the couplings among the antennas. In fact the undesired signals are usually much stronger than the tumor responses. A calibration signal is formed as an average of the signals containing similar strong undesired signals. Then the calibration signal is subtracted out from these signals to remove the undesired signals as much as possible. This simple removal method could be improved, but the residual of undesired content can be tolerated by our robust adaptive algorithm to some extent. Advanced methods such as those presented in [17] can be used here and a better performance may be achieved. Let $x_{i,j}(t)$ denote the signal after subtracting out the calibration signal.

In the second step, to process the signals coherently, we time-shift $x_{i,j}(t)$ by a number of samples $n_{i,j}(\mathbf{r}_0)$ to align the returns from the focal point (at location $\mathbf{r}_0$). The discrete time delays for the received signals can be determined from the corresponding transmitter and receiver locations $\mathbf{r}_{iT}$, $\mathbf{r}_{jR}$ and the imaging location of interest $\mathbf{r}_0$

$$n_{i,j}(\mathbf{r}_0) = \frac{1}{\Delta t}\left\lfloor \frac{\|\mathbf{r}_{iT} - \mathbf{r}_0\|}{c} + \frac{\|\mathbf{r}_{jR} - \mathbf{r}_0\|}{c} \right\rfloor \tag{1}$$

where $\lfloor x \rfloor$ stands for rounding to the greatest integer less than x, $\|\cdot\|$ denotes the Euclidean norm, c is the approximate velocity of the microwaves propagating in the normal breast tissues, and Δt is the sampling interval, which is assumed to be well below the Nyquist interval. Note that (1) assumes that the breast tissue is homogeneous, which in fact is not true. However, this approximation causes little performance degradations when used with our robust adaptive algorithm. Let $\hat{x}_{i,j}(t)$ be the time shifted signal. Then,

$$\begin{aligned}\hat{x}_{i,j}(\mathbf{r}_0, t) &= x_{i,j}(t + n_{i,j}(\mathbf{r}_0))\\ t &= -n_{i,j}(\mathbf{r}_0), \ldots, T - n_{i,j}(\mathbf{r}_0)\end{aligned} \tag{2}$$

where T is the maximum round-trip discrete-time delay required for a pulse to propagate from the transmitter to the skin or chest wall and back to the receiver. Hence T defines the maximum duration of interest of the received signal.

Next, we apply a time-window to the time-shifted signals. The window is given by

$$w(t) = \begin{cases} 1, & 0 < t < N - 1 \\ 0, & \text{otherwise} \end{cases} \tag{3}$$

where $N\Delta t$ is the approximate time duration of the backscattered signal from the focal point $\mathbf{r}_0$. Note that N is determined by the duration of the known transmitted pulse and the sampling interval. Let $\tilde{x}_{i,j}(\mathbf{r}_0, t), t = 0, \ldots, N-1$, denote the windowed signal.

Finally, we consider the effects of propagation attenuation in the lossy breast tissues. The major attenuation is caused by a decrease in the amplitude of the spherical wave as it expands. To eliminate this attenuation, we multiply each received signal by a suitable compensation factor. The compensation factor can be determined from the locations of the transmitter and receiver, $\mathbf{r}_{iT}$, $\mathbf{r}_{jR}$, and of the focal point, $\mathbf{r}_0$, as follows:

$$K_{i,j}(\mathbf{r}_0) = ||\mathbf{r}_{iT} - \mathbf{r}_0||^2 \cdot ||\mathbf{r}_{jR} - \mathbf{r}_0||^2 \tag{4}$$

Then the compensated signal $y_{i,j}(\mathbf{r}_0, t)$ is given by

$$y_{i,j}(\mathbf{r}_0, t) = K_{i,j}(\mathbf{r}_0)\tilde{x}_{i,j}(\mathbf{r}_0, t), \quad t = 0, \ldots, N-1. \tag{5}$$

We remark that since our problem is interference (due to undesired reflections) limited, rather than noise limited, the loss of SNR caused by the aforementioned attenuation compensation is insignificant.

III. MAMI

MAMI is a two-stage adaptive imaging method. First, the data-adaptive RCB algorithm is used spatially to obtain a vector of multiple backscattered waveforms for each probing signal. Second, RCB is employed to recover a scalar waveform based on the estimated vector of waveforms obtained in the first stage. The estimated scalar waveform is used to compute the backscattered energy $p(\mathbf{r}_0)$.

A. MAMI-Stage I

For notational simplicity, the dependence of $y_{i,j}(t, \mathbf{r}_0)$ on the generic location vector $\mathbf{r}_0$ is omitted in what follows. Consider the following model for the preprocessed signal vector:

$$\mathbf{y}_i(t) = \mathbf{a}(t)s_i(t) + \mathbf{e}_i(t), \quad \mathbf{y}_i(t) \in \mathbb{R}^{M\times 1} \tag{6}$$

where $\mathbf{y}_i(t) = [y_{i,1}(t), \ldots, y_{i,M}(t)]^T$. The scalar $s_i(t)$ denotes the backscattered signal (from the focal point at location $\mathbf{r}_0$) corresponding to the probing signal from the ith transmitting antenna. The vector $\mathbf{a}(t)$ in (6) is referred to as the array steering vector; note that $\mathbf{a}(t)$ is approximately equal to $\mathbf{1}_{M\times 1}$ since all the signals have been aligned temporally and their attenuations compensated for. The vector $\mathbf{e}_i(t)$ denotes the residual term at point $\mathbf{r}_0$, which includes the unmodeled noise and interference due to undesired reflections.

There are two assumptions with this model. First, we assume that the steering vector varies with t, and is nearly a constant with respect to i. Second, we assume that the backscattered signal waveform depends only on i but not on j, the jth receiving antenna. The truth, however, is that the steering vector is not exactly known and changes slightly with both t and i due to array calibration errors and other factors. The signal waveform should also vary with both i and j, due to the frequency-dependent lossy medium within the breast [27]. These assumptions simplify the problem slightly and cause little performance degradations when used with robust adaptive algorithms. By assuming that the true steering vector is time-varying, we allocate more “room” for robustness.

Due to the errors induced by waveform distortions, antenna location uncertainties, time-delay roundoffs, etc., the steering vector $\mathbf{a}(t_0)$ will be imprecise in practice, in the sense that the elements of $\mathbf{a}(t_0)$ may differ slightly from 1. This uncertainty in the steering vector motivates us to consider using RCB for waveform estimation. To make the paper as self-contained as possible, we give a review of the RCB algorithm. RCB is derived from the Standard Capon Beamforming (SCB) algorithm. SCB aims at estimating the signal waveform (or signal energy), by choosing a weight vector for the data, which minimizes the array output power and passes the signal of interest without any distortion. To improve the performance of SCB in the presence of steering vector errors and in the case of a low number of snapshots, RCB makes an explicit use of an uncertainty set for the array steering vector. Therefore, we assume that the true steering vector $\mathbf{a}(t_0)$ lies in the vicinity of the assumed steering vector $\bar{\mathbf{a}} = [1, \ldots, 1]^T$, and that the only knowledge we have about $\mathbf{a}(t_0)$ is that

$$||\mathbf{a}(t_0) - \bar{\mathbf{a}}||^2 \le \epsilon \tag{7}$$

where ϵ is used to describe the uncertainty of $\mathbf{a}(t_0)$ about $\bar{\mathbf{a}}$, the choice of which will be discussed later on.

In Stage I, for a given time t_0, $t_0 = 0, \ldots, N-1$, we can estimate the true steering vector $\mathbf{a}(t_0)$ via the following covariance fitting approach [23] of RCB

$$\begin{aligned} &\max_{\sigma^2(t_0), \mathbf{a}(t_0)} \sigma^2(t_0) \\ &\text{subject to}\, \hat{\mathbf{R}}_Y(t_0) - \sigma^2(t_0)\mathbf{a}(t_0)\mathbf{a}^T(t_0) \ge 0, \\ &\qquad ||\mathbf{a}(t_0) - \bar{\mathbf{a}}||^2 \le \epsilon \end{aligned} \tag{8}$$

where $\sigma^2(t_0) = 1/M \sum_{i=1}^{M} s_i^2(t_0)$ is the power of the “signal of interest,” and

$$\hat{\mathbf{R}}_Y(t_0) \triangleq \frac{1}{M}\mathbf{Y}(t_0)\mathbf{Y}^T(t_0) \tag{9}$$

is the sample covariance matrix with

$$\mathbf{Y}(t_0) = [\mathbf{y}_1(t_0), \mathbf{y}_2(t_0), \ldots, \mathbf{y}_M(t_0)], \quad \mathbf{Y}(t_0) \in \mathbf{R}^{M\times M}. \tag{10}$$

Observe that both the signal power $\sigma^2(t_0)$ and the steering vector $\mathbf{a}(t_0)$ are treated as unknowns in (8). Hence there is a “scaling ambiguity” between these two unknowns (see [28]), in the sense that $(\sigma^2(t_0), \mathbf{a}(t_0))$ and $(\sigma^2(t_0)/\alpha, \alpha^{1/2}\mathbf{a}(t_0))$ (for any $\alpha > 0$) give the same term $\sigma^2(t_0)\mathbf{a}(t_0)\mathbf{a}^T(t_0)$. To eliminate this ambiguity, we later impose the norm constraint

$$||\mathbf{a}(t_0)||^2 = M. \tag{11}$$

For any given $\mathbf{a}(t_0)$, the solution to (8) is [28]

$$\hat{\sigma}^2(t_0) = \frac{1}{\mathbf{a}^T(t_0)\hat{\mathbf{R}}_Y^{-1}\mathbf{a}(t_0)}. \tag{12}$$

Hence, (8) can be reduced to the following quadratic optimization problem with quadratic constraint:

$$\min_{\mathbf{a}(t_0)} \mathbf{a}^T(t_0)\hat{\mathbf{R}}_Y^{-1}(t_0)\mathbf{a}(t_0) \quad \text{subject to} \quad \|\mathbf{a}(t_0) - \bar{\mathbf{a}}\|^2 \leq \epsilon. \tag{13}$$

To exclude the trivial solution $\mathbf{a}(t_0) = 0$, we need to assume that the uncertainty parameter is sufficiently small

$$\epsilon < \|\bar{\mathbf{a}}\|^2. \tag{14}$$

To determine the solution of (13) under (14), we use the *Lagrange multiplier methodology* and consider the following function:

$$\mathcal{L}(\mathbf{a}(t_0), \lambda) = \mathbf{a}^T(t_0)\hat{\mathbf{R}}_Y^{-1}(t_0)\mathbf{a}(t_0) + \lambda\left(\|\mathbf{a}(t_0) - \bar{\mathbf{a}}\|^2 - \epsilon\right) \tag{15}$$

where $\lambda \geq 0$ is the real-valued Lagrange multiplier satisfying $\hat{\mathbf{R}}_Y^{-1}(t_0) + \lambda\mathbf{I} > 0$, so that (15) can be minimized with respect to $\mathbf{a}(t_0)$. For the unconstrained minimization of $\mathcal{L}(\mathbf{a}(t_0), \lambda)$, for a fixed λ, the solution is given by

$$\begin{aligned}\hat{\mathbf{a}}(t_0) &= \left[\frac{\hat{\mathbf{R}}_Y^{-1}(t_0)}{\lambda} + \mathbf{I}\right]^{-1}\bar{\mathbf{a}} \\ &= \bar{\mathbf{a}} - \left[\mathbf{I} + \lambda\hat{\mathbf{R}}_Y(t_0)\right]^{-1}\bar{\mathbf{a}}\end{aligned} \tag{16}$$

where the matrix inversion lemma [14] has been used to obtain the second equality. Let $\bar{\mathcal{S}}$ denote the uncertainty set defined in (7). It can be shown that the solution $\hat{\mathbf{a}}(t_0)$ belongs to the boundary of $\bar{\mathcal{S}}$ and, hence, satisfies

$$\|\hat{\mathbf{a}}(t_0) - \bar{\mathbf{a}}\|^2 = \epsilon. \tag{17}$$

By using (16) in (17), we can obtain the Lagrange multiplier as the solution to the constraint equation

$$\mathcal{G}(\lambda) = \left\|\left[\mathbf{I} + \lambda\hat{\mathbf{R}}_Y(t_0)\right]^{-1}\bar{\mathbf{a}}\right\|^2 = \epsilon. \tag{18}$$

Let the eigendecomposition of $\hat{\mathbf{R}}_Y(t_0)$ be

$$\hat{\mathbf{R}}_Y(t_0) = \mathbf{U}\mathbf{D}\mathbf{U}^T \tag{19}$$

where the columns of $\mathbf{U}$ are the eigenvectors of $\hat{\mathbf{R}}_Y(t_0)$ and the diagonal elements of the diagonal matrix $\mathbf{D}$, $d_1 \geq d_2 \geq \cdots \geq d_M$, are the corresponding eigenvalues. Here, the dependencies of $\mathbf{U}$ and $\mathbf{D}$ on t_0 are omitted for simplicity. Let $\mathbf{b} = \mathbf{U}^*\bar{\mathbf{a}}$ and b_i denote its ith element. Then, (18) can be rewritten as

$$\mathcal{G}(\lambda) = \sum_{n=1}^{M} \frac{|b_n|^2}{(1 + \lambda d_n)^2} = \epsilon. \tag{20}$$

Note that $\mathcal{G}(\lambda)$ is a monotonically decreasing function of λ. Also, it is clear that $\mathcal{G}(0) > \epsilon$ by (14), and $\lim_{\lambda\to\infty} \mathcal{G}(\lambda) = 0 < \epsilon$. Hence, there is a unique solution $\lambda > 0$ to (20), which can be solved efficiently, say, by the Newton's method. Inserting λ in (16), we readily determine the solution $\hat{\mathbf{a}}(t_0)$. To eliminate the aforementioned "scaling ambiguity," by (11), we replace the solution $\hat{\mathbf{a}}(t_0)$ with

$$\hat{\hat{\mathbf{a}}}(t_0) = \frac{M^{1/2}\hat{\mathbf{a}}(t_0)}{\|\hat{\mathbf{a}}(t_0)\|}. \tag{21}$$

To obtain the signal waveform, we apply a weight vector to the received signals. The weight vector is determined by using the estimated steering vector $\hat{\hat{\mathbf{a}}}(t_0)$ in the weight vector expression formula of SCB (see, e.g., [28]). The weight vector used in Stage I of MAMI has the form given by

$$\begin{aligned}&\hat{\mathbf{w}}_{\mathrm{MAMI}_1}(t_0) \\ &= \frac{\hat{\mathbf{R}}_Y^{-1}(t_0)\hat{\hat{\mathbf{a}}}(t_0)}{\hat{\hat{\mathbf{a}}}^T(t_0)\hat{\mathbf{R}}_Y^{-1}(t_0)\hat{\hat{\mathbf{a}}}(t_0)} &(22) \\ &= \frac{\|\hat{\mathbf{a}}(t_0)\|}{M^{1/2}} \cdot \frac{\left[\hat{\mathbf{R}}_Y(t_0) + \frac{1}{\lambda}\mathbf{I}\right]^{-1}\bar{\mathbf{a}}}{\bar{\mathbf{a}}^T\left[\hat{\mathbf{R}}_Y(t_0) + \frac{1}{\lambda}\mathbf{I}\right]^{-1}\hat{\mathbf{R}}_Y(t_0)\left[\hat{\mathbf{R}}_Y(t_0) + \frac{1}{\lambda}\mathbf{I}\right]^{-1}\bar{\mathbf{a}}}. &(23)\end{aligned}$$

The equality to obtain (23) is due to inserting (16) and (21) in (22). Note that (23) has a diagonal loading form. Diagonal loading is a popular approach to mitigate the performance degradations of SCB in the presence of steering vector errors or small sample size problems. The distinction between RCB and the conventional diagonal loading methods is that RCB directly determines the optimal diagonal loading level needed for a given steering vector uncertainty set. Note that by diagonal loading, we can even allow the sample covariance matrix to be rank-deficient.

The beamformer output can be written as a vector

$$\hat{\mathbf{s}}(t_0) = \left[\hat{\mathbf{w}}_{\mathrm{MAMI}_1}^T(t_0)\mathbf{Y}(t_0)\right]^T, \quad \hat{\mathbf{s}}(t_0) \in \mathbb{R}^{M\times 1}. \tag{24}$$

Here, $\hat{\mathbf{s}}(t_0)$ contains the waveform estimates at t_0 of the backscattered signals (from the focal point $\mathbf{r}_0$) due to all the probing signals indexed from 1 to M. Repeating the above process from $t_0 = 0$ to $t_0 = N - 1$, we obtain the complete multiple backscattered signal waveform estimates.

Note that, at this stage, we have obtained M estimates of the backscattered waveforms corresponding to the probing signals sent by each of the transmitting antenna. Since these probing signals are UWB pulses with the same waveform, we can assume that the backscattered signal waveforms from $\mathbf{r}_0$ due to all the probing signals are (nearly) identical. To estimate the backscattering energy $p(\mathbf{r}_0)$ coherently, in the next stage, a scalar waveform $\{\hat{s}(t)\}_{t=0}^{N-1}$ is recovered from these estimated M-dimensional signal waveform vectors $\{\hat{\mathbf{s}}(t_0)\}_{t_0=0}^{N-1}$.

B. MAMI-Stage II

In the second stage of MAMI, the signal waveform vector $\hat{\mathbf{s}}(t), t = 0, \ldots, N-1$, is treated as a snapshot from an M-element (fictitious) "array"

$$\hat{\mathbf{s}}(t) = \mathbf{a}_s s(t) + \mathbf{e}_s(t), \quad t = 0, \ldots, N-1 \tag{25}$$

where $\mathbf{a}_s$ is approximately equal to $\mathbf{1}_{M\times 1}$ for the same reason as in Stage I. However, the "steering vector" $\mathbf{a}_s$ may again be imprecise, and hence RCB is needed again. In (25), $s(t)$ denotes the nominal backscattered signal waveform, due to all probing signals, and each element of $\mathbf{e}_s(t)$ contains the differences between the corresponding element in $\hat{\mathbf{s}}(t)$ and $s(t)$. Paralleling the description of Stage I, we estimate $s(t)$ via the following RCB formulation:

$$\max_{\tilde{\sigma}^2, \mathbf{a}_s} \tilde{\sigma}^2 \quad \text{subject to} \quad \hat{\mathbf{R}}_s - \tilde{\sigma}^2 \mathbf{a}_s \mathbf{a}_s^T \geq 0, \quad \|\mathbf{a}_s - \bar{\mathbf{a}}\|^2 \leq \tilde{\epsilon}, \tag{26}$$

where $\tilde{\sigma}^2 = 1/N \sum_{t=0}^{N-1} s^2(t)$ is the power of the signal of interest, $\tilde{\epsilon}$ is a user parameter, and $\hat{\mathbf{R}}_s$ is the following temporal sample covariance matrix:

$$\hat{\mathbf{R}}_s \triangleq \frac{1}{N} \sum_{t=0}^{N-1} \hat{\mathbf{s}}(t) \hat{\mathbf{s}}^T(t). \tag{27}$$

Note that here we can use the same assumed steering vector as in Stage I. To eliminate the scaling ambiguity, we again impose the norm constraint

$$\|\mathbf{a}_s\|^2 = M. \tag{28}$$

Similarly to Stage I, the solution $\hat{\mathbf{a}}_s$ to (26) is

$$\hat{\mathbf{a}}_s = \left(\frac{\hat{\mathbf{R}}_s^{-1}}{\nu} + \mathbf{I} \right)^{-1} \bar{\mathbf{a}} \tag{29}$$

where ν is the corresponding Lagrange multiplier used in solving (26), which can be determined similarly to obtaining λ. Similar to (28), we replace $\hat{\mathbf{a}}_s$ with

$$\hat{\hat{\mathbf{a}}}_s = \frac{M^{1/2} \hat{\mathbf{a}}_s}{\|\hat{\mathbf{a}}_s\|}. \tag{30}$$

Therefore, the adaptive weight vector $\hat{\mathbf{w}}_{\mathrm{MAMI}_2}$ for Stage II is determined by a formula similar to (23)

$$\hat{\mathbf{w}}_{\mathrm{MAMI}_2} = \frac{\hat{\mathbf{R}}_s^{-1} \hat{\hat{\mathbf{a}}}_s}{\hat{\hat{\mathbf{a}}}_s^T \hat{\mathbf{R}}_s^{-1} \hat{\hat{\mathbf{a}}}_s} \tag{31}$$

$$= \frac{\|\hat{\mathbf{a}}_s\|}{M^{1/2}} \cdot \frac{(\hat{\mathbf{R}}_s + \frac{1}{\nu}\mathbf{I})^{-1} \bar{\mathbf{a}}}{\bar{\mathbf{a}}^T (\hat{\mathbf{R}}_s + \frac{1}{\nu}\mathbf{I})^{-1} \hat{\mathbf{R}}_s (\hat{\mathbf{R}}_s + \frac{1}{\nu}\mathbf{I})^{-1} \bar{\mathbf{a}}} \tag{32}$$

where (32) shows again the diagonal loading form of the weight vector.

The weighted output is the estimate $\hat{s}(t)$ of $s(t)$

$$\hat{s}(t) = \hat{\mathbf{w}}_{\mathrm{MAMI}_2}^T \hat{\mathbf{s}}(t). \tag{33}$$

Finally, the backscattered energy for the focal point $\mathbf{r}_0$ is computed as

$$p(\mathbf{r}_0) \triangleq \sum_{t=0}^{N-1} \hat{s}^2(t). \tag{34}$$

In summary, the MAMI method can be described as follows.

Step 1: Preprocess the received signal, i.e., remove the unwanted content, time-shift, apply the time-window and compensate for the propagation loss.

Step 2: From the preprocessed signals, obtain multiple backscattered signal waveform estimates $\hat{\mathbf{s}}(t)$ via RCB.

Step 3: Estimate the scalar waveform $\hat{s}(t)$ from $\hat{\mathbf{s}}(t)$ via RCB. Finally compute the backscattered energy via (34).

For RCB used in Stages I and II of MAMI, the choice of ϵ and $\tilde{\epsilon}$ should be made as small as possible. It can be experimentally observed that as ϵ or $\tilde{\epsilon}$ increases, the resolution of RCB decreases. When ϵ or $\tilde{\epsilon}$ is large, the ability of RCB to suppress interferences that are close to the signal of interest degrades. Also, the smaller the sample size N or the larger the steering vector and the system errors, the larger should ϵ and $\tilde{\epsilon}$ be chosen [23], [24]. Such qualitative guidelines are usually sufficient for the choice of uncertainty size parameters, as the performance of RCB dose not depend very critically on them (as long as they take on "reasonable values") [28]. In our numerical examples, we choose two reasonable initial values of them and then make adjustment experimentally to obtain the best image quality.

Regarding the computational complexity of MAMI, the major computational cost of MAMI is due to RCB used in Stages I and II. The major flop count of using RCB comes from the eigen-decomposition of the sample covariance matrices [23], [24] ($\hat{\mathbf{R}}_Y(t_0)$ for Stage I and $\hat{\mathbf{R}}_s$ for Stage II), each requiring $O(M^3)$ flops. Also, RCB is used N times in Stage I and once in Stage II. Hence MAMI requires $O(M^3N)$ flops for a given focal point, which is larger than the $O(M^2N)$ flops of DAS.

IV. Numerical Examples

A. Breast Model and Data Acquisition

In our numerical examples, we consider a 3-D simulated breast model. Two cross sections of the model are shown in Fig. 2. The 3-D model includes randomly distributed fatty breast tissue, glandular tissue, 2-mm-thick skin, as well as the nipple and chest wall. To reduce the reflections from the skin, the breast model is immersed in a lossless liquid with permittivity similar to that of the breast fatty tissue. The breast is a hemisphere with 100 mm in diameter. A 6 mm-diameter

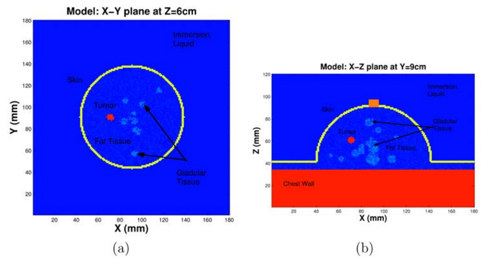

Fig. 2. Cross sections of a 3-D hemisphere breast model at (a) $z = 60$ mm and (b) $y = 90$ mm.

TABLE I
NOMINAL DIELECTRIC PROPERTIES OF BREAST TISSUES

Tissues	Dielectric Properties	
	Permittivity (F/m)	Conductivity (S/m)
Immersion Liquid	9	0
Chest Wall	50	7
Skin	36	4
Fatty Breast Tissue	9	0.4
Nipple	45	5
Glandular Tissue	11-15	0.4-0.5
Tumor	50	4

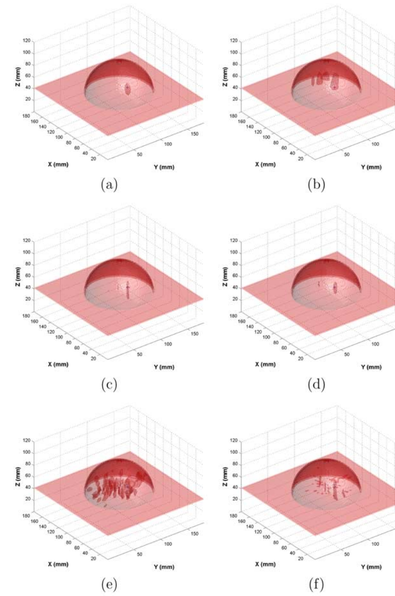

Fig. 3. Comparison of 3-D images of a 6 mm in diameter tumor obtained via six different imaging algorithms, in the absence of thermal noise. The intensity scale is logarithmic with a 20-dB dynamic range. The shaded hemisphere is the contour of the breast, and the dotted shades inside correspond to the intensity of the backscattered energy estimates. (a) MAMI with $\epsilon = \tilde{\epsilon} = 2.4$, (b) multistatic DAS, (c): RCB, (d) APES, (e) MIST, and (f) monostatic DAS.

tumor (a 4 mm-diameter tumor at the same location will be treated in our fourth example) is located 27 mm under the skin (at $x = 70$ mm, $y = 90$ mm, $z = 60$ mm). The diameter of the tumor is larger than that of the smallest 2–mm-diameter tumor considered in the literature [17]. However, the smaller tumor considered there was for a 2-D model, which is equivalent to an infinitely long cylindrical tumor in the 3-D model. Thus it has significantly larger backscattered energy in the FDTD simulations than our spherical tumor in the 3-D model.

The dielectric properties of the breast tissues are assumed to be Gaussian random variables with variations of $\pm 10\%$ around their nominal values. This variation represents the upper bound reported in the literature [3], [6]. The nominal values are chosen to be typical of the reported data [3]–[7], which is given in Table I. The dielectric constants of glandular tissues are between $\varepsilon_r = 11$ and $\varepsilon_r = 15$. Since the transmitted signal is an UWB pulse, the dispersive properties of the fatty breast tissue and those of the tumor are also considered in the model. The frequency dependencies of permittivity $\varepsilon(\omega)$ and conductivity $\sigma(\omega)$ are modeled by the single-pole Debye model [13]. The randomly distributed breast tissues with variable dielectric properties are representative of the nonhomogeneity of the breast from an actual patient.

As shown in Fig. 1, a hemispherical antenna array consisting of $M = 72$ omnidirectional antennas is used, with each antenna being approximated as a point source. The antennas are 1 cm away from the breast skin, on $P = 6$ layers in the z-axis dimension. The layers of the antenna are arranged along the z-axis between 5.0 cm and 7.5 cm, with 0.5-cm spacing between the layers. Within each layer, $Q = 12$ antennas are placed on a cross-sectional circle with uniform spacing.

The UWB signal used in our simulations is a Gaussian pulse, with the pulse interval being about 120 ps. The spectrum of this source waveform has a peak near 5 GHz. The probing signals are emitted by each of the 72 antennas sequentially. For each probing signal, the backscattered signals are recorded by all the antennas, resulting in 72 received backscattered signals. We use the FDTD method in our simulations to obtain the backscattered signals. The grid cell size used by FDTD is 1 mm $\times$ 1 mm $\times$ 1 mm and the time step is 1.667 ps (about 600-GHz sampling frequency). The model is terminated according to perfectly match layer absorbing boundary conditions [29]–[31]. The Z transform [32], [33] is used to implement the FDTD method whenever materials with frequency-dependent properties are involved. Finally, the length of the time window in the preprocessing step is 150 samples, therefore $N = 150$ for each of the preprocessed signal.

B. Imaging Results

In this section, several numerical examples are provided to demonstrate the performance of MAMI under various conditions. For comparison purposes, the multistatic DAS scheme presented in [15], and several monostatic methods, namely RCB [14], APES [34], [35], MIST [17], and the monostatic DAS [13] (see Table II), are also applied to the same datasets. The monostatic and multistatic DAS are simple schemes that estimate the signal waveform $s(t)$ using the data-independent weight vector

$$\hat{\mathbf{w}}_{\mathrm{DAS}} = \frac{\bar{\mathbf{a}}}{M}. \tag{35}$$

Then the estimated backscattered signal waveform for the monostatic case is

$$\hat{s}_{\mathrm{monostaticDAS}}(t) = \hat{\mathbf{w}}_{\mathrm{DAS}}^T \tilde{\mathbf{y}}(t) \tag{36}$$

TABLE II
VARIOUS MEASUREMENTS OF FIG. 3

Methods	Tumor location (x, y, z) (mm) True location: (70, 90, 60) (mm)	FWHM tumor size (mm^3)	SCR (dB)
MAMI	70, 90, 59	$4 \times 5 \times 13$	35.9
Multistatic DAS	70, 90, 60	$7 \times 7 \times 12$	11.1
RCB	68, 90, 56	$3 \times 4 \times 21$	9.1
APES	70, 90, 60	$4 \times 4 \times 6$	11.7
MIST	70, 90, 60	$13 \times 9 \times 16$	3.0
Mono-static DAS	69, 90, 57	$2 \times 5 \times 21$	1.1

where $\tilde{\mathbf{y}}(t)$ is a vector consisting of all the diagonal elements of $\mathbf{Y}(t)$. For the multistatic case,

$$\hat{s}_{\text{multistaticDAS}}(t) = \hat{\mathbf{w}}_{\text{DAS}}^T \mathbf{Y}(t) \hat{\mathbf{w}}_{\text{DAS}}. \quad (37)$$

MIST uses a data-independent weight vector that is designed to pass the backscattered signals from $\mathbf{r}_0$ with unit gain and attenuate signals from other locations [17]. We have generalized the 2-D algorithm in [17] to the 3-D case. APES and RCB [14] are data-adaptive approaches for monostatic or bistatic microwave imaging.

Fig. 3 shows the 3-D images obtained via MAMI and the aforementioned methods. Fig. 4 shows the corresponding X-Y and X-Z cross section images. The images are displayed on a logarithmic scale with a 20-dB dynamic range. In Fig. 3(a) as well as in 4(a1) and 4(a2), which correspond to MAMI, the tumor is conspicuously shown at the true location in the X-Y plane, with negligible clutter. The resolution in the X-Z plane is poorer due to the geometry of the array. The images obtained with the other methods are poorer or much poorer than the MAMI images. Note that the images in Figs. 3(c)–(f) and 4(c1)–(f2) are worse than those in [14]. The reason is that the antennas in our examples are away from the breast skin, instead of being on the skin as in [14]. Consequently the strengths of the tumor responses in our examples are lower than those in the examples of [14]. In all the numerical examples, the user parameters ϵ and $\tilde{\epsilon}$ are adjusted to obtained the best image quality. Note that the resolution in the z direction is poorer than those in the x and y directions, due to the geometry of our array (the array aperture is smaller in the X-Z dimension than in its X-Y counterpart.)

The second example shows the imaging results when additive Gaussian noise with zero-mean and variance σ_0^2 is added to the data in Example 1. The signal-to-noise ratio (SNR) is defined as

$$\text{SNR} = 10 \log_{10} \left\{ \frac{\frac{1}{M^2} \sum_{i=1}^{M} \sum_{j=1}^{M} \left[\frac{1}{T} \sum_{t=0}^{T-1} \check{E}_{i,j}^2(t) \right]}{\sigma_0^2} \right\} \text{dB}, \quad (38)$$

The $\check{E}_{i,j}(t)$ in (38) is the received signal due to the tumor only, which is not available in practice. Hence, to compute the SNR, we performed the simulation twice, with and without the tumor, and took the difference of the two received signals as an approximation to $\check{E}_{i,j}(t)$. In the preprocessing, a simple low-pass filter is applied to the raw data to remove some noise.

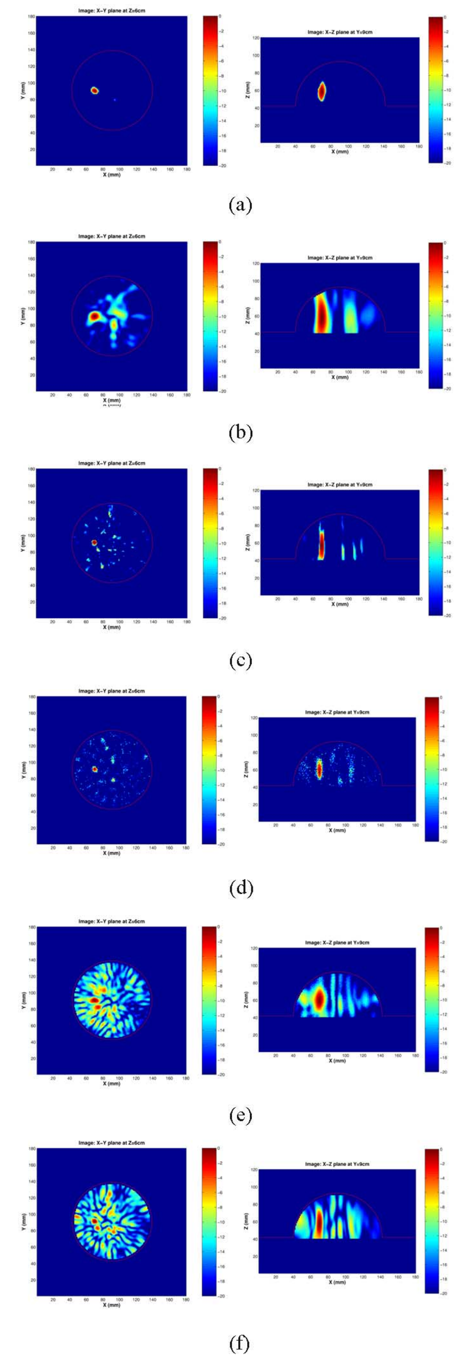

Fig. 4. Comparison of cross sections of the images in Fig. 3. The intensity scale is logarithmic with a 20-dB dynamic range. (a1) and (a2) MAMI with $\epsilon = \tilde{\epsilon} = 2.4$, (b1) and (b2) multistatic DAS, (c1) and (c2): RCB, (d1) and (d2) APES, (e1) and (e2) MIST, and (f1) and (f2) monostatic DAS.

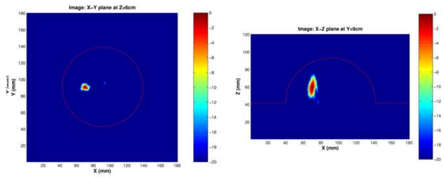

(a)

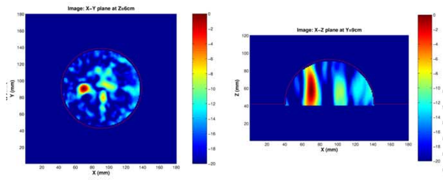

(b)

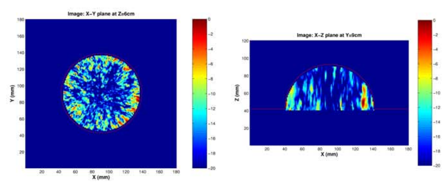

(c)

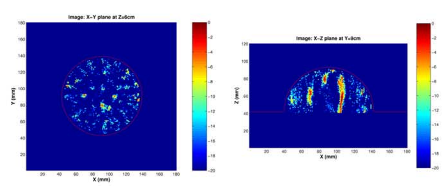

(d)

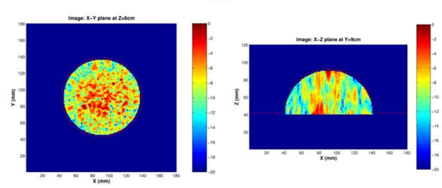

(e)

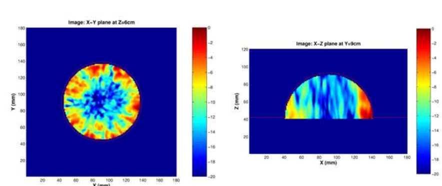

(f)

Fig. 5. Comparison of the cross section images obtained via six imaging algorithms. A 6 mm-diameter tumor is present with thermal noise added to yield $\mathrm{SNR} = -22\ \mathrm{dB}$. The intensity scale is logarithmic with a 20-dB dynamic range. (a1) and (a2) MAMI with $\epsilon = \tilde{\epsilon} = 2.4$, (b1) and (b2) multistatic DAS, (c1) and (c2) RCB, (d1) and (d2) APES, (e1) and (e2) MIST, and (f1) and (f2) monostatic DAS.

The noise suppression capability of MAMI is demonstrated in Fig. 5, where $\mathrm{SNR} = -22\ \mathrm{dB}$. At such a low SNR, the received tumor responses are completely buried in noise. Note from Fig. 5(a1) and (a2) that MAMI can still produce quite clear images, with the tumor only slightly blurred by noise. The other methods perform much worse. In particular, in all monostatic images, the tumor is completely buried in the noise and clutter. This superior performance of MAMI demonstrates the effectiveness of the two-stage RCB scheme in suppressing the noise. We also varied SNR in our numerical experiments, and as expected, the image quality of all imaging methods degrade with decreased SNR.

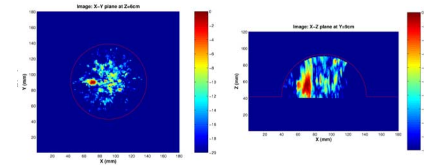

(a)

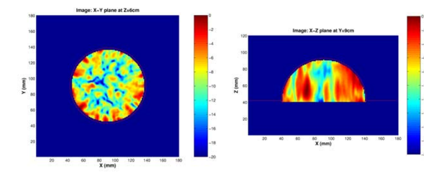

(b)

Fig. 6. Comparison of the cross section images obtained using MAMI and multistatic DAS for 18 antennas. A 6 mm-diameter tumor is present with thermal noise added to yield $\mathrm{SNR} = -22\ \mathrm{dB}$. Presented on a log magnitude with a 20-dB dynamic range. (a1) and (a2) MAMI with $\epsilon = \tilde{\epsilon} = 2.4$, and (b1) and (b2) multistatic DAS.

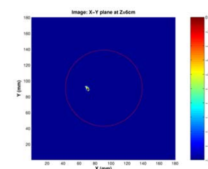

(a)

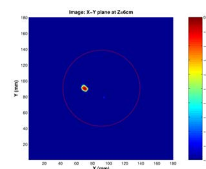

(b)

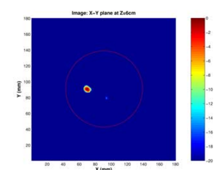

(c)

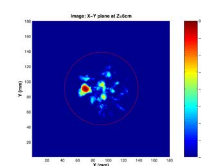

(d)

Fig. 7. Images of 6 mm-diameter tumor obtained via MAMI with different ϵ and $\tilde{\epsilon}$. The intensity scale is logarithmic with a 20-dB dynamic range. (a) $\epsilon = \tilde{\epsilon} = 0.6$, (b) $\epsilon = \tilde{\epsilon} = 1.8$, (c) $\epsilon = \tilde{\epsilon} = 2.4$, and (d) $\epsilon = \tilde{\epsilon} = 3.6$.

In the third example, the number of antennas is decreased to one quarter of the original number: only 18 antennas are used, arranged on the same hemisphere as before. The original 6 layers of antennas are reduced to 3 layers in that every other layer is eliminated; for each remaining layer, the original 12 antennas are reduced to 6 antennas in that every other antenna is eliminated. Again, the thermal noise is added, with $\mathrm{SNR} = -22\ \mathrm{dB}$. In the practical imaging system design, the size of the antenna array is one of the most important concerns: due to the limited available space around the breast, a small number of antennas is desirable. Yet reducing the antenna number poses a challenge to any imaging methods, due to the greatly reduced amount of information for imaging. Fig. 6(a) and (a2) show the cross section images produced by MAMI. The tumor stands out by more than 10 dB compared to the neighboring clutter and interference. In Fig. 6(b1) and (b2), which are produces by multi-

TABLE III
VARIOUS MEASUREMENTS OF THE 2-D X-Y CROSS SECTION IMAGES IN FIG. 4–8

Cases		MAMI	Multi-static DAS	RCB	APES	MIST	Mono-static DAS
6 mm tumor	Tumor location	69, 90	69, 90	69, 90	69, 91	69, 90	69, 91
	FWHM (mm)	4×5	6×7	4×5	4×3	13×9	4×5
	SCR (dB)	30.1	12.8	11.9	12.3	4.4	6.3
6 mm tumor, noisy	Tumor location	69, 90	69, 90	69, 91	103, 50	80, 86	109, 133
	FWHM (mm)	4×4	6×7	3×3	1×3	3×3	8×9
	SCR (dB)	29.8	12.4	3.3	0.5	0.6	0.0
4 mm tumor	Tumor location	69, 90	69, 90	66, 90	104, 111	82, 74	78, 92
	FWHM (mm)	4×5	13×7	4×4	1×1	4×5	5×5
	SCR (dB)	10.9	4.6	3.8	2.9	1.1	0.7

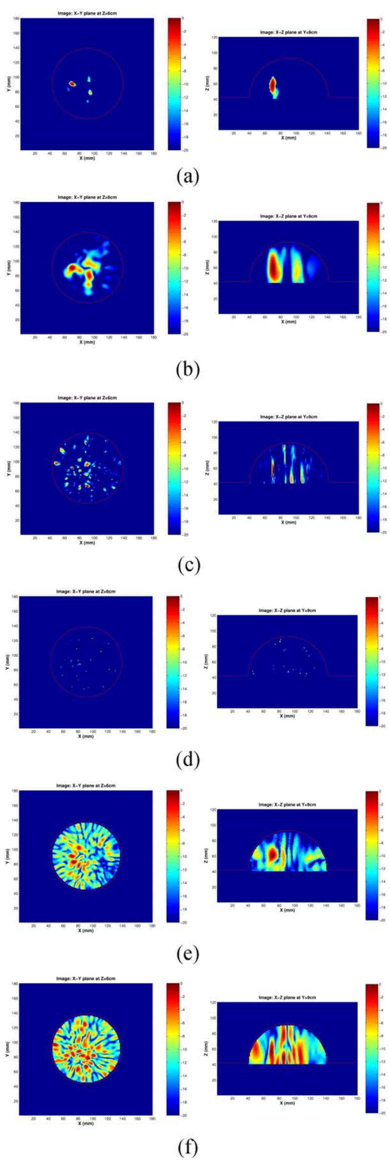

Fig. 8. Cross section images in the presence of a 4 mm-diameter tumor, in the absence of thermal noise, and with 72 antennas. The intensity scale is logarithmic with a 20-dB dynamic range. (a1) and (a2) MAMI with $\epsilon = \tilde{\epsilon} = 2.4$, (b1) and (b2) multistatic DAS, (c1) and (c2) RCB, (d1) and (d2) APES, (e1) and (e2) MIST, and (f1) and (f2) monostatic DAS.

static DAS, the tumor is complete buried in clutter. The quality of the images produced by MAMI using 18 antennas is comparable to that corresponding to the best monostatic methods using 72 antennas.

In the fourth example, we vary ϵ and $\tilde{\epsilon}$. Fig. 7(a)–(c) shows the images of the 6-mm-diameter tumor formed by MAMI with different ϵ and $\tilde{\epsilon}$ (here we choose $\epsilon = \tilde{\epsilon}$ for simplicity). We note that the image quality does not vary significantly with ϵ and $\tilde{\epsilon}$.

The fifth example is similar to the first one except that the tumor size is now reduced to 4 mm in diameter. The backscattered microwave energy is much smaller in this case since the backscattered energy from tumor is proportional to the square of the tumor diameter. Fig. 8(a1) and (a2) show the MAMI images, where the tumor is still observable, about 10 dB higher than the neighboring clutter. The other methods, as shown in Fig. 8(b1)–(f2), give much poorer performance.

We measure the tumor localization accuracy based on the maximum pixel value in the image, and measure the tumor size based on the full-width at half-maximum the tumor response [20]. To quantify the image quality, we use the signal-to-clutter ratio [20], which is defined as the ratio of the maximum tumor response to the maximum clutter value in the same image. The maximum clutter value is determined as the maximum pixel value outside the volume containing the tumor. Such measurements for the images in Figs. 3–8 are summarized in Tables II and III.

V. CONCLUSION

We have considered adaptive multistatic microwave imaging for breast cancer detection. A real aperture array is used for data collection. Each antenna in the array takes turns to transmit an ultra-wideband pulse while all antennas receive the backscattered signals. The data-adaptive algorithm, referred to as the MAMI algorithm, is a two-stage robust Capon beamforming algorithm. Using a 3-D breast model simulated via the finite-difference time-domain (FDTD) method, we have shown that MAMI exhibits higher resolution, lower sidelobes, and better noise and interference rejection capability than other existing approaches.

ACKNOWLEDGMENT

The authors would like to thank Mr. W. Roberts for his helpful comments on the paper.

REFERENCES

[1] E. C. Fear, S. C. Hagness, P. M. Meaney, M. Okoniewski, and M. A. Stuchly, "Enhancing breast tumor detection with near-field imaging," *IEEE Microw. Magazine*, vol. 3, no. 1, pp. 48–56, Mar. 2002.

[2] S. J. Nass, I. C. Henderson, and J. C. Lashof, *Mammography and Beyond: Developing Techniques for the Early Detection of Breast Cancer*. Washington, D.C: Inst. Med., Nat. Acad. Press, 2001.

[3] S. S. Chaudhary, R. K. Mishra, A. Swarup, and J. M. Thomas, "Dielectric properties of normal and malignant human breast tissues at radiowave and microwave frequencies," *Indian J.f Biochem. Biophys.*, vol. 21, pp. 76–79, Feb. 1984.

[4] A. J. Surowiec, S. S. Stuchly, J. R. Barr, and A. Swarup, "Dielectric properties of breast carcinoma and the surrounding tissues," *IEEE Trans. Biomed. Eng.*, vol. 35, no. 4, pp. 257–263, Apr. 1988.

[5] A. Swarup, S. S. Stuchly, and A. J. Surowiec, "Dielectric properties of mouse MCA1 fibrosarcoma at different stages of development," *Bioelectromagnetics*, vol. 12, no. 1, pp. 1–8, 1991.

[6] W. T. Joines, Y. Zhang, C. Li, and R. L. Jirtel, "The measured electrical properties of normal and malignant human tissues from 50 to 900 mhz," *Med. Phys.*, vol. 21, pp. 547–550, Apr. 1994.

[7] C. Gabriel, R. W. Lau, and S. Gabriel, "The dielectric properties of biological tissues: II. measured in the frequency range 10 Hz to 20 GHz," *Phys. Med. Biol.*, vol. 41, pp. 2251–2269, Nov. 1996.

[8] K. L. Carr, "Microwave radiometry: Its importance to the detection of cancer," *IEEE Trans. Microw. Theory Tech.*, vol. 37, no. 12, pp. 1862–1869, Dec. 1989.

[9] B. Bocquet, J. C. van de Velde, A. Mamouni, Y. Leroy, G. Giaux, J. Delannoy, and D. Del Valee, "Microwaves radiometric imaging at 3 GHz for the exploration of breast tumors," *IEEE Trans. Microw. Theory Tech.*, vol. 38, no. 6, pp. 791–793, Jun. 1990.

[10] L. V. Wang, X. Zhao, H. Sun, and G. Ku, "Microwave-induced acoustic imaging of biological tissues," *Rev. Scientif. Instrum.*, vol. 70, pp. 3744–3748, 1999.

[11] P. M. Meaney, M. W. Fanning, D. Li, S. P. Poplack, and K. D. Paulsen, "A clinical prototype for active microwave imaging of the breast," *IEEE Trans. Microw. Theory Tech.*, vol. 48, no. 11, pp. 1841–1853, Nov. 2000.

[12] A. E. Souvorov, A. E. Bulyshev, S. Y. Semenov, R. H. Svenson, and G. P. Tatsis, "Two-demensional computer analysis of a microwave flat antenna array for breast cancer tomography," *IEEE Trans. Microw. Theory Tech.*, vol. 48, no. 8, pp. 1413–1415, Aug. 2000.

[13] X. Li and S. C. Hagness, "A confocal microwave imaging algorithm for breast cancer detection," *IEEE Microw. Wireless Compon. Lett.*, vol. 11, no. 3, pp. 130–132, Mar. 2001.

[14] B. Guo, Y. Wang, J. Li, P. Stoica, and R. Wu, "Microwave imaging via adaptive beamforming methods for breast cancer detection," *J. Electromagn. Waves Applicat.*, vol. 20, no. 1, pp. 53–63, 2006.

[15] R. Nilavalan, A. Gbedemah, I. J. Craddock, X. Li, and S. C. Hagness, "Numerical investigation of breast tumour detection using multi-static radar," *Inst. Elect. Eng. Electron. Lett* vol. 39, Dec. 2003, Online No. 20031183.

[16] I. J. Craddock, R. Nilavalan, J. Leendertz, and A. Preece, "Experimental investigation of real aperture synthetically organised radar for breast cancer detection," in *Proc. IEEE Antennas and Propagation Symp.*, Jul. 2005, vol. 1B, pp. 179–182.

[17] E. J. Bond, X. Li, S. C. Hagness, and B. D. Van Veen, "Microwave imaging via space-time beamforming for early detection of breast cancer," *IEEE Trans. Antennas Propagat.*, vol. 51, no. 8, pp. 1690–1705, Aug. 2003.

[18] S. K. Davis, E. J. Bond, S. C. Hagness, and B. D. Van Veen, "Microwave imaging via space-time beamforming for early detection of breast cancer: Beamforming design in the frequency domain," *J. Electromagn. Waves Applicat.*, vol. 17, pp. 357–381, Feb. 2003.

[19] E. C. Fear and M. A. Stuchly, "Microwave detection of breast cancer," *IEEE Trans. Microw. Theory Tech.*, vol. 48, no. 11, pp. 1854–1863, Nov. 2000.

[20] E. C. Fear, X. Li, S. C. Hagness, and M. A. Stuchly, "Confocal microwave imaging for breast cancer detection: Localization of tumors in three dimensions," *IEEE Trans. Biomed. Eng.*, vol. 49, no. 8, pp. 812–822, Aug. 2002.

[21] E. C. Fear and M. Okoniewski, "Confocal microwave imaging for breast cancer detection: Application to hemispherical breast model," in *Dig., 2002 IEEE MTT-S Int. Microwave Symp.* , Jun. 2002, vol. 3, pp. 1759–1762.

[22] M. A. Hernández-López, M. Quintillán-González, S. G. García, A. R. Bretones, and R. G. Martín, "A rotating array of antennas for confocal microwave breast imaging," *Microw. Opt. Technol. Lett.*, vol. 39, pp. 307–311, Nov. 2003.

[23] J. Li, P. Stoica, and Z. Wang, "On robust capon beamforming and diagonal loading," *IEEE Trans. Signal Process.*, vol. 51, no. 7, pp. 1702–1715, Jul. 2003.

[24] P. Stoica, Z. Wang, and J. Li, "Robust capon beamforming," *IEEE Signal Process. Lett.*, vol. 10, no. 6, pp. 172–175, Jun. 2003.

[25] A. Taflove and S. C. Hagness, *Computational Electrodynamics: The Finite-Difference Time-Domain Method*, 3rd ed. Boston, MA: Artech House, 2005.

[26] D. M. Sullivan, *Electromagnetic Simulation Using FDTD Method*, 1st ed. Piscataway, NJ: Wiley–IEEE Press, 2000, RF and Microwave Technology.

[27] P. Kosmas, C. M. Rappaport, and E. Bishop, "Modeling with the FDTD method for microwave breast cancer detection," *IEEE Trans. Microw. Theory Tech.*, vol. 52, no. 8, pp. 1890–1897, Aug. 2004.

[28] J. Li and P. Stoica, Eds., Robust Adaptive Beamforming New York, Wiley, 2005.

[29] S. D. Gedney, "An anisotropic perfectly matched layer-absorbing medium for the truncation of FDTD lattices," *IEEE Transactions on Antennas and Propagation*, vol. 44, pp. 1630–1639, Dec. 1996.

[30] J. P. Berenger, "A perfectly matched layer for the absorption of electromagnetic waves," *J. Comput. Phys.*, vol. 114, pp. 185–200, Oct. 1994.

[31] Z. S. Sacks, D. M. Kingsland, R. Lee, and J. F. Lee, "A perfectly matched anisotropic absorber for use as an absorbing boundary condition," *IEEE Trans. Antennas Propagat.*, vol. 43, no. 12, pp. 1460–1463, Dec. 1995.

[32] D. M. Sullivan, "Frequency-dependent FDTD methods using Z transforms," *IEEE Trans. Antennas Propagat.*, vol. 40, no. 10, pp. 1223–1230, Oct. 1992.

[33] ——, "Z-transform theory and the FDTD method," *IEEE Trans. Antennas Propagat.*, vol. 44, no. 1, pp. 28–34, Jan. 1996.

[34] J. Li and P. Stoica, "An adaptive filtering approach to spectral estimation and SAR imaging," *IEEE Trans. Signal Process.*, vol. 44, no. 6, pp. 1469–1484, Jun. 1996.

[35] P. Stoica, H. Li, and J. Li, "A new derivation of the APES filter," *IEEE Signal Process. Lett.*, vol. 6, no. 8, pp. 205–206, Aug. 1999.

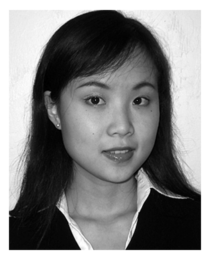

Yao Xie (S'04) received the B.Sc. degree from the University of Science and Technology of China (USTC), Hefei, China, in 2004, and the M.Sc. degree from the University of Florida, Gainesville, in 2006, both in electrical engineering. She is currently working towards the Ph.D. degree in the Department of Electrical Engineering, Stanford University, Stanford, CA.

Her research interests include signal processing, medical imaging, and optimization.

Ms. Xie is a member of Tau Beta Pi and Etta Kappa Nu. She was the first place winner in the Student Best Paper Contest at the 2005 Annual Asilomar Conference on Signals, Systems, and Computers, for her work on breast cancer detection.

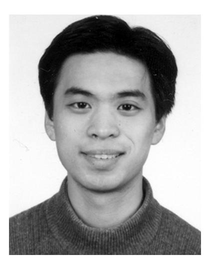

Bin Guo (S'06) received the B.E. and M.Sc. degree in electrical engineering from Xian Jiaotong University, Xian, China, in 1997 and 2000 respectively. He is working towards the Ph.D. degree in electrical engineering in the Department of Electrical and Computer Engineering, University of Florida, Gainesville.

From April 2002 to July 2003, he was an Associate Research Scientist with the Temasek Laboratories, National University of Singapore, Singapore. Since August 2003, he has been a Research Assistant with the Department of Electrical and Computer Engineering, University of Florida. His current research interests include biomedical applications of signal processing, microwave imaging, and computational electromagnetics.

Luzhou Xu (S'05) received the B.Eng. and M.S. degrees in electrical engineering from Zhejiang University, Hangzhou, China, in 1996 and 1999, respectively. He is currently working towards the Ph.D. degree in the Department of Electrical and Computer Engineering, University of Florida, Gainesville.

From 1999 to 2001, he was with the Zhongxing RD institute, Shanghai, China, where he was involved in the system and algorithm design of mobile communications equipment. From 2001 to 2003, he was with Wireless Communications Group, Philips Research, Shanghai. His research interests include statistical signal processing and its applications.

Jian Li (S'88–M'90–SM'97–F'05) received the M.Sc. and Ph.D. degrees in electrical engineering from The Ohio State University, Columbus, in 1987 and 1991, respectively.

From July 1991 to June 1993, she was an Assistant Professor with the Department of Electrical Engineering, University of Kentucky, Lexington. Since August 1993, she has been with the Department of Electrical and Computer Engineering, University of Florida, Gainesville, where she is currently a Professor. Her current research interests include spectral estimation, statistical and array signal processing, and their applications.

Dr. Li is a fellow of Institution of Electrical Engineers (IEE). She received the 1994 National Science Foundation Young Investigator Award and the 1996 Office of Naval Research Young Investigator Award. She has been a member of the Editorial Board of *Signal Processing*, a publication of the European Association for Signal Processing (EURASIP), since 2005. She is presently a member of two of the IEEE Signal Processing Society technical committees: the Signal Processing Theory and Methods (SPTM) Technical Committee and the Sensor Array and Multichannel (SAM) Technical Committee.

Petre Stoica (SM'91–F'94) received the D.Sc. degree in automatic control from the Polytechnic Institute of Bucharest (BPI), Bucharest, Romania, in 1979 and an honorary doctorate degree in science from Uppsala University (UU), Uppsala, Sweden, in 1993.

He is a Professor of Systems Modeling with the Division of Systems and Control, the Department of Information Technology, UU. He was a Professor of System Identification and Signal Processing with the Faculty of Automatic Control and Computers, BPI. He held longer visiting positions with Eindhoven University of Technology, Eindhoven, The Netherlands; Chalmers University of Technology, Gothenburg, Sweden (where he held a Jubilee Visiting Professorship); UU; The University of Florida, Gainesville, FL; and Stanford University, Stanford, CA. His main scientific interests are in the areas of system identification, time series analysis and prediction, statistical signal and array processing, spectral analysis, wireless communications, and radar signal processing. He has published nine books, ten book chapters, and some 500 papers in archival journals and conference records. The most recent book he coauthored, with R. Moses, is *Spectral Analysis of Signals* (Prentice-Hall, 2005). He is on the editorial boards of six journals: *Journal of Forecasting, Signal Processing, Circuits, Signals, and Signal Processing, Digital Signal Processing, ICA Review Journal, Signal Processing Magazine*, and *Multidimensional Systems and Signal Processing*. He was a co-guest editor for several special issues on system identification, signal processing, spectral analysis, and radar for some of the aforementioned journals, as well as for the *IEE Proceedings*.

Dr. Stoica was corecipient of the IEEE ASSP Senior Award for a paper on statistical aspects of array signal processing. He was also recipient of the Technical Achievement Award of the IEEE Signal Processing Society. In 1998, he was the recipient of a Senior Individual Grant Award of the Swedish Foundation for Strategic Research. He was also co-recipient of the 1998 EURASIP Best Paper Award for Signal Processing for a work on parameter estimation of exponential signals with time-varying amplitude, a 1999 IEEE Signal Processing Society Best Paper Award for a paper on parameter and rank estimation of reduced-rank regression, a 2000 IEEE Third Millennium Medal, and the 2000 W. R. G. Baker Prize Paper Award for a paper on maximum likelihood methods for radar. He was a member of the international program committees of many topical conferences. From 1981 to 1986, he was a Director of the International Time-Series Analysis and Forecasting Society, and he was also a member of the IFAC Technical Committee on Modeling, Identification, and Signal Processing. He is also a member of the Royal Swedish Academy of Engineering Sciences, an honorary member of the Romanian Academy, and a fellow of the Royal Statistical Society.